Nanoscale

Accepted Manuscript

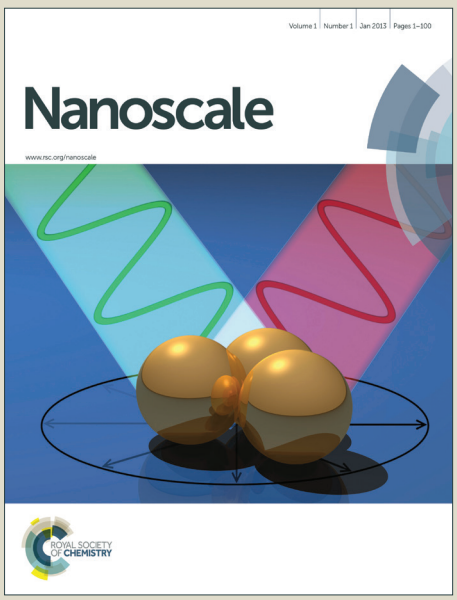

ROYAL SOCIETY OF CHEMISTRY

www.rsc.org/nanoscale

Cite this: DOI: 10.1039/c0xx00000x

www.rsc.org/xxxxxx

ARTICLE TYPE

Facile Synthesis of One-dimensional Mn_3O_4/Zn_2SnO_4 Hybrid Composites and Their High Performance as Anodes for LIBs

*Ranran Zhang, Yanyan He, Aihua Li and Liqiang Xu**

Received (in XXX, XXX) Xth XXXXXXXXX 20XX, Accepted Xth XXXXXXXXX 20XX
DOI: 10.1039/b000000x

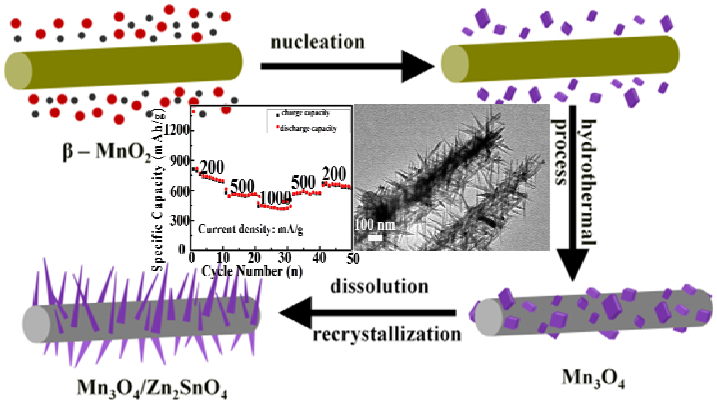

One-dimensional (1D) Mn_3O_4 nanorod /Zn_2SnO_4 nanoneedle hierarchical composites have been conveniently synthesized via a simple hydrothermal process at 180 °C for 24 h. It is found that the reaction time and appropriate amount of ammonia play vital roles during their formation processes，and their formation is likely driven by the lattice match of the cubic Zn_2SnO_4 nanoneedle and cubic Mn_3O_4 nanorod. The as-obtained composites deliver a high initial discharge capacity of 1370.9 mAh g^{-1} at 100 mA g^{-1} in the region of 0.01-3.0 V，and a reversible specific capacity of 577.4 mAh g^{-1} could be retained after 50 cycles. It is note that 441.5 mAh g^{-1} could be maintained after 50 cycles even if the current density was set as high as 1000 mAh g^{-1}, and the rate performance of nanocomposites (200, 500, 1000 mA g^{-1}) also shows excellent reversible character. The high specific capacity, good cycling stability and high rate performance of the as-obtained composites enable them to be promising and competitive high-performance anode in lithium-ion batteries (LIBs). It is worth noting that the fabrication method reported here can be easily extended to prepare other 1D metal oxide hybrid materials including $Mn_3O_4/ZnFe_2O_4$, $Mn_2O_3/CoFe_2O_4$ and $Mn_2O_3/NiFe_2O_4$ composites via a similar hydrothermal process with/without subsequent calcinations, which hold great promise for their wide potential applications in energy, catalysis and environmental science and technology.

Introduction

One-dimensional (1D) hybrid complex nanostructures based on different metal oxides have been widely studied in recent years not only because they could retain and integrate the basic characteristics of the individual components, but also could impart unique multifunctionality.[1, 2] More importantly, some interesting synergetic new effects can usually be generated by the 1D hybrid materials, which endow them with obviously improved performances in diversified applications such as in catalysis, environment and energy related areas, for instance, the discharge capacity of TiO_2-C/MnO_2 nanowire electrodes after 100 cycles is 352 mAh g^{-1}, which is higher than that of TiO_2 (130 mAh g^{-1}) and TiO_2/C (162 mAh g^{-1});[3] $SnO_2/ZnWO_4$ core-shell nanorods have reversible capacity of 1000 mAh g^{-1} at small current density of C/20 rate higher than that of pure $ZnWO_4$, SnO_2, or the traditional theoretical result of their simple mixture;[4] 1D mesoporous TiO_2 nanobelts and graphene sheets deliver a high reversible capacity of over 430 mA h g^{-1} at a low current density of 0.15 A g^{-1}.[5] All these studies indicate that introducing synergistic effects of 1D hybrid nanostructures is a good approach to enhance the reversible capacity of individual nanostructure-based LIB anodes, whereas

rational design and develop new kinds of 1D hybrid nanostructures with high performances in LIBs still remains a great challenge.

Very recently, Sn based binary oxide materials have drawn considerable attention as one kind of the most promising negative-electrode materials for LIBs owing to their low lithium insertion potentials, high volumetric and gravimetric capacities.[6] Among them, inverse spinel-type Zn_2SnO_4, is one kind of multifunctional material, which can not only be widely used as photovoltaic devices, combustible gases and humidity detection, photoeletrochemisty, functional coatings and transparent conducting electrodes, but also can be utilized as promising anode material for lithium ion batteries (with the theoretical irreversible capacity of 1231 mAh g^{-1}). [7] To date, Zn_2SnO_4 nanomaterials of various morphologies, including single nanostructure or nanocomposites, have been synthesized by diverse methods and used as anode materials in LIBs. For instance, cubic Zn_2SnO_4 materials obtained by a solid state reaction have a specific discharge capacity of 689 mAh g^{-1} after 50 cycles at the current density of 50 mA g^{-1};[8] Hollow Zn_2SnO_4 nanoboxes prepared via the hydrothermal process has reversible capacity of 540 mAh g^{-1} at a current density of 300 mA g^{-1} after 45 cycles;[9] Flower-like Zn_2SnO_4 composites prepared through a hydrothermal synthesis has a reversible capacity of 501mAh g^{-1} at a current density of 300 mA g^{-1} after 50 cycles；[10] Zn_2SnO_4/C composite materials fabricated via the combined hydrothermal and carbothermic reduction process show a reversible capacity of above 560 mAh g^{-1} after 40 cycles at a current density of 60 mA g^{-1}.[11] Carboncoated Zn_2SnO_4 nanomaterials synthesized by a hydrothermal method has a reversible capacity of 400mAh g^{-1} at a current density of 300 mA g^{-1} after 40 cycles；[12] Hollow Zn_2SnO_4@graphene (GN) composites prepared by co-precipitation and alkali etching method show a reversible capacity 752.9 mAh g^{-1} at 300 mA g^{-1} after 45 cycles；[13] Recently, hollow Zn_2SnO_4@PPY composites synthesized through a micro emulsion polymerization have the reversible capacity of 478.4 mAh g^{-1} after 50 cycles at a current density of 60 mA g^{-1}.[14] In addition, Zn_2SnO_4/MnO_2 core/shell nanocable-carbon microfiber hybrid composites applied for supercapacitor electrodes also display high performance；[15] Nevertheless, the electrochemical features of all these Zn_2SnO_4 materials especially their cycling stability and capacity retention are far away from satisfaction. In addition, the synthesis and electrochemical property of 1D Zn_2SnO_4 hybrid composites have rarely been reported. As is known that manganese oxides (MnO_x) deliver the advantages of a high theoretical capacity (MnO_2 ~1232 mAh g^{-1}, Mn_3O_4 ~937 mAh g^{-1}), relatively low electromotive force, natural abundance, low cost and environmental benignity, etc, therefore, they are of great application potential in composite anode materials as a functional enhancement support.[16]

In this study, 1D Mn_3O_4/Zn_2SnO_4 composites that are composed of Mn_3O_4 nanorods (as the back-bone with lengths in the range of 2-10 μm and the average diameter of 50 nm) and Zn_2SnO_4 nanoneedles (as the branches with the average lengths about 200 nm) have been conveniently synthesized by using $Zn(CHCOO)_2{\cdot}2H_2O$, $Na_2SnO_3{\cdot}4H_2O$ and β-MnO_2 nanorods (as templates) as reactants via a hydrothermal process at 180 °C for 24 h. β-MnO_2 has been transformed into Mn_3O_4 by ammonia after the hydrothermal process. To the best of our knowledge, such 1D composite built by Mn_3O_4 and Zn_2SnO_4 subunits has not been reported and explored as anodes previously. Their formation is proved to be driven by the lattice match of the cubic Zn_2SnO_4 nanoneedle and cubic Mn_3O_4 nanorod. The as-obtained sample has initial discharge-charge capacities of 1370.9 mAh g^{-1} and 817.6 mAh g^{-1} at a current density of 100 mA g^{-1} in the voltage about 0.01-3.0 V. After 50 cycles, a reversible capacity of 577.4 mAh g^{-1} can be remained with the coulombic efficiency of 97.16%, revealing its superior capacity retention ability compared with most of the previous reported Zn_2SnO_4 individual materials and nanocomposites. The obviously improved capacity retention and rate capability make 1D hybrid structure a promising and competitive alternative for anode materials in LIBs. Besides the Mn_3O_4 nanorod /Zn_2SnO_4 nanoneedle composites, it is worth noting that Mn_3O_4/Zn_2SnO_4, $Mn_2O_3/CoFe_2O_4$ and $Mn_2O_3/NiFe_2O_4$ hybrid composites could also be obtained via the similar fabrication approach with or without the subsequent calcinations, which proves that the present method is a general strategy for the controllable synthesis of novel hybrid composites based on lattice match growth mechanism. The method provides new opportunities to further propel the structure designation, property regulation and potential applications of new kinds of fascinating hybride materials and great promise for their potential applications in energy, catalysis and environmental science and technology.

Experiential Section

Materials

$Zn(CHCOO)_2{\cdot}2H_2O$, $Na_2SnO_3{\cdot}4H_2O$, $FeCl_3{\cdot}6H_2O$, $ZnCl_2$, $NH_3{\cdot}H_2O$, ethanol absolute, urea, Sodium carboxymethyl cellulose (1200 mpa). All the raw materials used here were of analytic grade without further purification.

Experimental Section

The synthesis of 1D Mn_3O_4/Zn_2SnO_4 nanocomposites was started from the β-MnO_2 nanorods. [17] The as-prepared β-MnO_2 nanorods (80 mg) with 25 mL

deionized water were firstly ultrasonicated for 30 min and then were stirred for another 30 min. Then, 0.2 M Zn $(CHCOO)_2{\cdot}2H_2O$ (10 mL) and 0.18 M $Na_2SnO_3{\cdot}4H_2O$ (10 mL) were added into the above solution. After it is stirred for 30 min, 8 mL $NH_3{\cdot}H_2O$ were dropped slowly. Last, the mixed solution was continually stirred for 1h before transferred into a Teflon-lined autoclave with a capacity of 60 mL. The autoclave was heated from room temperature to 180 °C and maintained at 180 °C for 24 h. In addition, in order to study the influence of reaction time and the amount of $NH_3{\cdot}H_2O$, different reaction time (6, 12, 18h) and different amount of $NH_3{\cdot}H_2O$ (0, 16 mL) were also studied while keeping other experimental conditions unchanged. The resulting 1D branched Mn_3O_4/Zn_2SnO_4 product was collected by centrifugation and washed repeatedly with anhydrous ethanol and distilled water for several times. Finally, it was dried in vacuum at 60°C for 12 h.

Apparatus

X-ray powder diffraction (XRD) patterns of the sample were obtained from a Bruker D8 advanced X-ray diffractometer that was equipped with graphite-monochromated $Cu_{K\alpha}$ radiation (λ= 1.5418Å). The Fourier transform infrared spectroscopy (FT-IR) spectrum instrument used here was a Bruker VERTEX 70 with a resolution of 4 cm^{-1}. TEM images were taken on a JEM-2100 microscope. The high resolution images and STEM images were recorded using a high resolution transmission electron microscope (HRTEM, JEOL-2100F) operated at 200 kV. Particle morphology images were recorded using a field-emission scanning electron microscope (FESEM, JEOL JSM-6700 M) with energy-dispersive X–ray (EDX) spectroscopy and an EDX mapping system (30 kV). The BET surface area (SBET) and Barrett–Joyner–Halenda (BJH) pore size distribution (PSD) were characterized by a QuadraSorb SI surface area analyzer (version 5.06); Surface analysis of the studied samples was performed using XPS (VGESCA-LABMK X-ray photoelectronic spectrometer).

Electrochemical testing

The electrochemical discharge-charge performances of the samples were tested on a Land battery test system (CT2001A) at 25°C. The working electrodes were consisted of 75 wt% active materials, 15 wt% carbon black, and 10 wt% CMC. Distilled water was used as the solvent. The mixed slurry with thickness of 200 μm was coated onto a piece of copper foil and dried in vacuum oven at 60°C for 12 h, then cut into discs with diameter of 12 mm. And the mass calculation of the active Zn_2SnO_4 materials was carried out based on 75% of the mass of electrode piece. Nickel foams were used as the current collector, and Celgard 2300 microporous polypropylene membrane was used as the separator. The electrolyte was composed of 1 mol /L LiPF6 dissolved ethylene carbonate/dimethyl carbonate/diethyl carbon-ate (EC/DMC/DEC, volume ratio was 1:1:1). Lithium foils with the diameter of 15 mm and the thickness of 0.4 mm were used as the counter electrodes. The button batteries were assembled in an argon-filled glove box, and cycled at different charge-discharge current densities (100, 500, 1000 mA g^{-1}) within voltage limit of 0.01V—3.00V using a Land battery test system (CT2001A, China) at room temperature (25 °C). The cyclic voltammetry (CV) profiles was measured a LK2005A Electrochemical Workstation in the region of 0.01-3.0 V at a scan rate of 0.1 mV s^{-1}.

Results and discussion

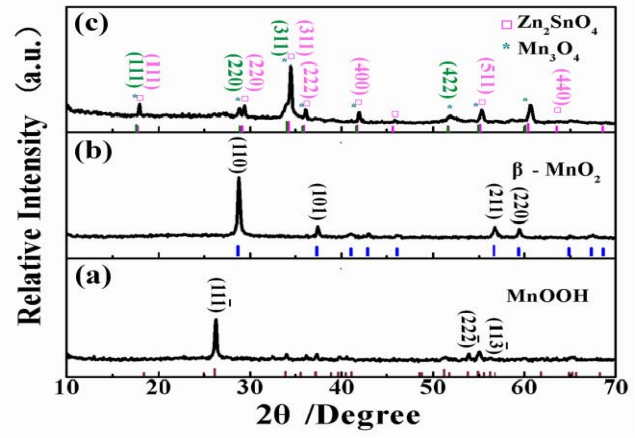

Fig. 1 XRD patterns of a) MnOOH nanorods, b) β-MnO_2 nanorods, c) 1D branched Mn_3O_4/Zn_2SnO_4 composites prepared at 180 °C for 24 h (8 mL $NH_3{\cdot}H_2O$).

Fig. 1c shows the XRD pattern of the final product and the diffraction peaks marked with purple square are indexed to the inverse spinel-type Zn_2SnO_4 (JCPDS card no. 24-1470), and the diffraction peaks marked with green star can be indexed as the Mn_3O_4 (space group $Fd\bar{3}m$; JCPDS card no. 04-0732). It can be seen that the initial MnOOH nanorods (space group *P*21/c14; JCPDS card no. 41-1379; Fig. 1a) transformed into tetragonal-phase β-MnO_2 (JCPDS card no. 24-0735; Fig. 1b) after the calcinations. When 0 or 16 mL $NH_3{\cdot}H_2O$ was used, the diffraction peaks of $MnSn_2$ (Fig. S1, Supporting Information) were found co-existed with Zn_2SnO_4 and Mn_3O_4. The FTIR analyses result evidences the existence of the Zn_2SnO_4 and Mn_3O_4. [18] The specific surface area of the product is 48.65 m^2/g (Fig. S2, Supporting Information). The full XPS spectrum of the product is shown in Fig. 2a. Fig. 2(b, c) demonstrate the existence of Zn^{2+} and Sn^{4+}, respectively. Little satellite structure could also be observed in Fig.2d. After refined fitting, the spectrum in 653.1 eV can be deconvoluted into two peaks. Among them, 655.1 eV can be assigned to the

existence of Mn (II), while the other peak at 652. 7 eV are characteristic of the Mn (III) cation, which is in agreement with the reported reference data on Mn_3O_4.[19]

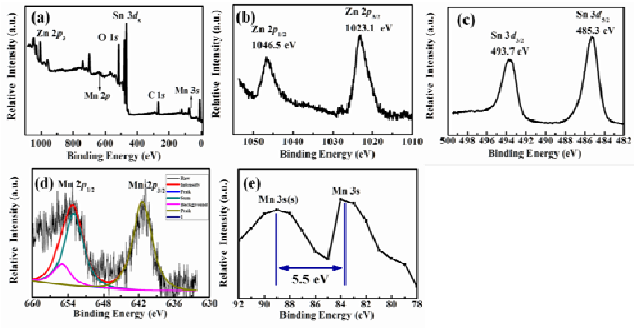

Fig.2 XPS spectra: (a) survey spectrum, (b) Zn 2p, (c) Sn 3d, (d) Mn 2p and (e) Mn 3s for 1D branched composites prepared at 180 °C for 24 h (8 mL $NH_3{\cdot}H_2O$).

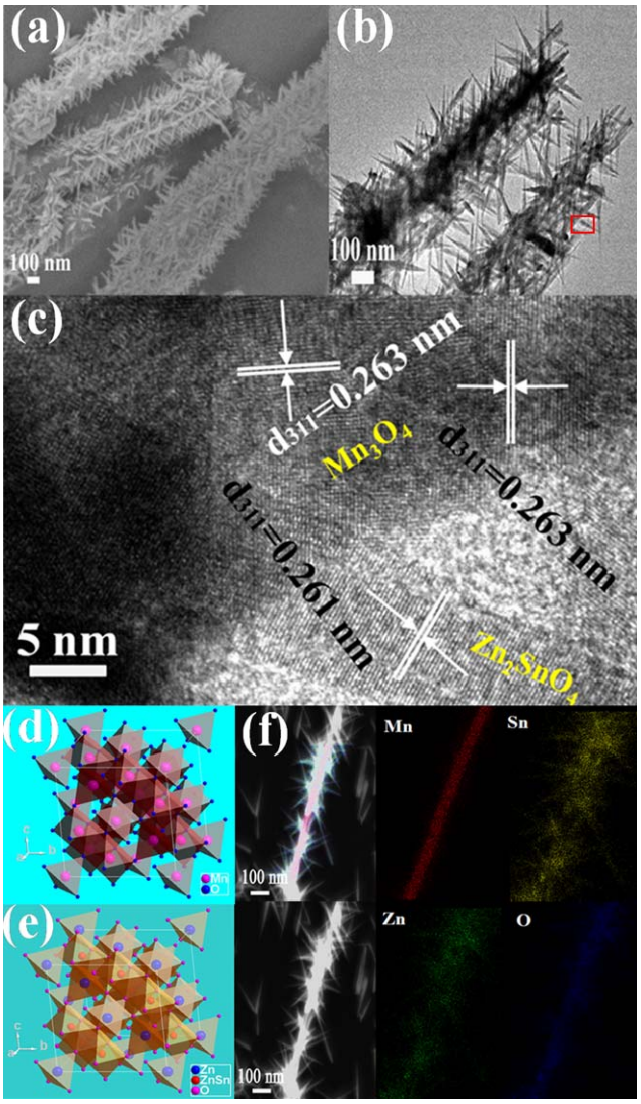

Fig. 3 (a, b) FESEM and TEM images of 1D branched Mn_3O_4/Zn_2SnO_4 composites prepared at 180 °C for 24 h (8 mL $NH_3{\cdot}H_2O$); (c) HRTEM image of 1D branched Mn_3O_4/Zn_2SnO_4 composites marked with red square; (d, e) crystal structures of Zn_2SnO_4 and Mn_3O_4, respectively; (f) STEM images of an individual 1D branched Mn_3O_4/Zn_2SnO_4 composites.

It is observed from Fig. 3 (a, b) that larger quantities of Zn_2SnO_4 nanoneedles attached on Mn_3O_4 nanorods to form 1D branched composites. From the magnified image in Fig. 3c, one can clearly see that numerous Zn_2SnO_4 nanoneedles with similar sizes (the average lengths about 200 nm) tightly and monodispersely root from the Mn_3O_4 nanorod along all directions. Fig. 3d displays the HRTEM images of part area of the 1D branched Mn_3O_4/Zn_2SnO_4 composites that marked with red square in Fig. 3c. The lattice fringe spacings of 0.261 and 0.263 nm can be ascribed to the (311) plane of inverse spinel-type Zn_2SnO_4 and (311) plane of Mn_3O_4, respectively. The HRTEM observation result is in agreement with that of the XRD analysis. As Zn_2SnO_4 and Mn_3O_4 have the same crystal system (cubic), space group ($Fd\bar{3}m$, No. 227) and approaching lattice parameters (Zn_2SnO_4: a=8.657 Å, b=8.657 Å, c=8.657 Å; Mn_3O_4: a=8.7 Å, b=8.7 Å, c=8.7 Å). The lattice mismatch is only ~0.5%. Therefore, it can be concluded that the Zn_2SnO_4 tend to nucleate and grow epitaxial on the side (311) planes of these Mn_3O_4 nanorods, mainly owing to lattice matching. [16] On the other hand, to reduce the total surface energy of the whole reaction system,[20] large amount of Zn_2SnO_4 nanoparticles tend to attach on the surface of Mn_3O_4 nanorods. As a result, with the increasing reaction time, 1D branched Mn_3O_4/Zn_2SnO_4 composites are finally formed. The crystal structures of Zn_2SnO_4 and Mn_3O_4 (towards (311) planes) are displayed in Fig. 3(d, e), respectively. Fig. 3f displays the STEM images of an individual 1D branched Mn_3O_4/Zn_2SnO_4 composite, which can distinguish the phases of Zn_2SnO_4 and Mn_3O_4 clearly. The SAED pattern and EDX spectrum (Fig. S3, Supporting Information) of the as-obtained 1D composites were also investigated and the results confirm the co-existence of Zn_2SnO_4 and Mn_3O_4. The FESEM and TEM images of the as-obtained MnOOH and β-MnO_2 are shown in Fig. S4 (Supporting Information).

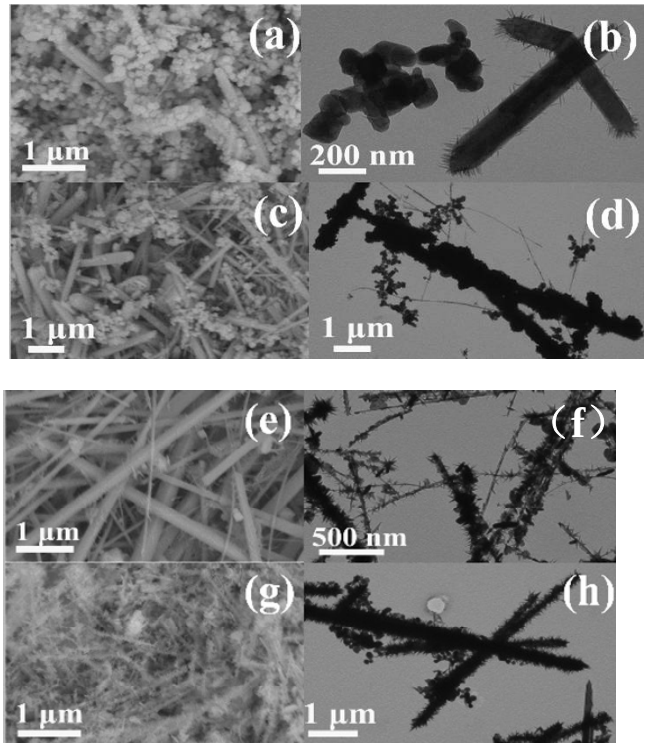

Fig. 4 FESEM and TEM images of the product obtained at 180°C for different reaction time: (a, b) 6 h, (c, d) 12 h, (e, f) 18 h, and (g, h) 24 h.

$$2Zn^{2+} + Sn^{4+} + 8OH^- \rightarrow Zn_2SnO_4 + 4H_2O \quad (1)$$

$$9MnO_2 + 4NH_3 \rightarrow 3Mn_3O_4 + 2N_2 + 6H_2O \quad (2)$$

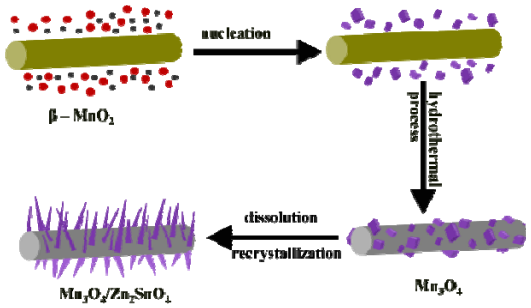

Scheme 1 Schematic illustration of the formation of 1D branched Mn_3O_4/Zn_2SnO_4 composites.

The growth process of the 1D branched Mn_3O_4/Zn_2SnO_4 composite is illustrated in Scheme 1. Firstly, the nanocrystalline Zn_2SnO_4 were formed under the hydrothermal process due to the precipitation reaction according to equation 1. Then, a large number of tiny nanocrystals began to nucleate and form irregular cubes; At the same time, β-MnO_2 was reduced to Mn_3O_4 by ammonia (equation 2). Then, the newly produced irregular cubes possessed high surface energies tended to aggregate randomly on the surface of the Mn_3O_4 nanorods. With the increasing reaction time, the irregular cubes tended to transform into nanoneedles owing to dissolution and recrystallization. Afterward, those differently oriented Zn_2SnO_4 nanoneedles would self-assembly to grow into 1D branched Mn_3O_4/Zn_2SnO_4 composite to reduce the total surface energy through Ostwald ripening process. Moreover, time-dependent experiments were carried out at 180°C and the intermediate complexes were inspected by SEM and TEM (Fig. 4), from which the continued growth process of the composites can be clearly seen.

Very recently, metal ferrite based materials also show obvious advantages and promising applications as anodes for lithium ion batteries.[21, 22] In this experiment, it is worth noting that besides the controllable synthesis of 1D Mn_3O_4/Zn_2SnO_4 composite (with relative stable structures at high currents, Fig. S5), Mn_3O_4 nanorod/$ZnFe_2O_4$ nanosheet (Fig. S6 and S7, which have a discharge capacity of 1232.7 mAh g^{-1} after 230 cycles at a current density of 1000 mA g^{-1}), $Mn_2O_3/CoFe_2O_4$ hybrid composites (Fig. S8 and S9, which have a discharge capacity of 881.8 mAh g^{-1} after 114 cycles and 1029.1 mAh g^{-1} after 260 cycles at a current density of 500 and 1000 mA g^{-1}, respectively.) and $Mn_2O_3/NiFe_2O_4$ (Fig. S10 and 11) could also be produced with high yield via the similar route, and their 1D shape is still remained after subsequent calcinations. The as-obtained metal ferrite based composites show superior cycle performances compared with the those of the previous reports (Tab. S1 and S2). Therefore, the method described here provide a general new avenue for the facile synthesis and property improvement of series of novel metal oxide hybrid composites, which hold great promise for their new promising applications in energy storage, catalysis and environmental science and technology.

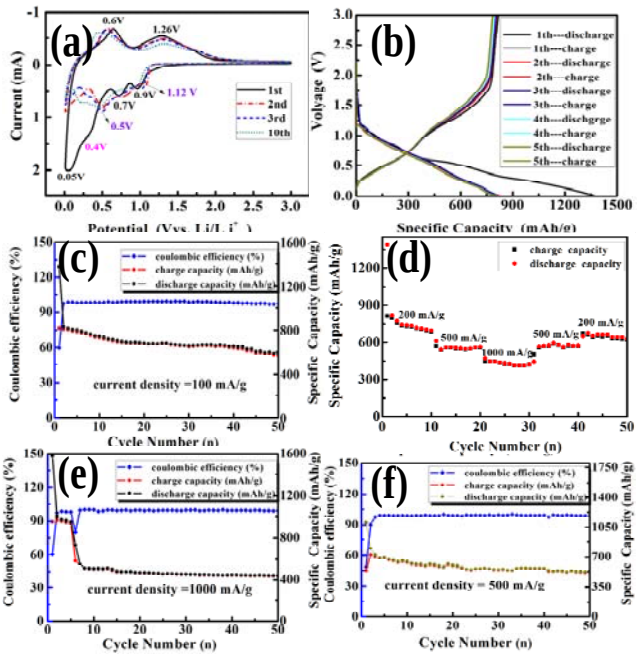

Fig. 5 (a) Cyclic voltammograms of the Mn_3O_4/Zn_2SnO_4 sample electrode at a scan rate of 0.1 mV s^{-1} in the region of 0.01-3.0 V (versus Li/Li^+); (b) Typical

discharge–charge curves for selected cycles at a current density of 100 mA/g and (c) corresponding discharge/charge capacity and coulombic efficiency; (d) The rate performance of the composite electrode; (e, f) discharge/charge capacity and coulombic efficiency at a current density of 500 and 1000 mA g^{-1}, respectively.

The redox peak position of Mn_3O_4/Zn_2SnO_4 composite electrode in the first cycle curve (Fig. 5a) is in good agreement with the first charge-discharge voltage platform (Fig. 5b), which is consistent with those of the previous reports.[23] Fig. 5c displays the corresponding cycling performance of the Mn_3O_4/Zn_2SnO_4/Li button battery at 100 mA g^{-1}. The first discharge-charge capacities of the Mn_3O_4/Zn_2SnO_4 nanorods composites are 1370.9 and 817.6 mAh g^{-1}. After 50 cycles, the specific capacity can remain at 577.4 mAh g^{-1} and the coulombic efficiency of each cycle is above 97.16%. The rate capacity of the Mn_3O_4/Zn_2SnO_4 composites (Fig. 5d) shows the lowest discharge capacity of 432 mAh g^{-1} at a current density of 1 mA g^{-1}, which is higher than the theoretical specific capacity of graphene. Upon altering the current density back to 100 mA g^{-1}, the discharge capacity could recover to 653 mAh g^{-1}, revealing rather high cycle stability. Fig. 5(e, f) show the cycling performances of the electrode at high current densities (500 and 1000 mA g^{-1}). It can be seen in Fig. 5e that the charge–discharge capacities of the sample maintained a stable trend before 50 cycles with a discharge capacity of 529.9 mAh g^{-1}. When the current density was increased to 1000 mA g^{-1}, the electrode can still retain a discharge capacity of 441.5 mAh g^{-1} for the 50th cycle.

Table 1. Comparison between the 1D branched Mn_3O_4/Zn_2SnO_4 composites and previously reported Zn_2SnO_4 structures.

Material	Reversible capacity (mAh/g)	Current density (mA/g)	Cycle number (n)	Ref.
Zn_2SnO_4 nanoparticles	342	100	40	18
Zn_2SnO_4 hollow box	540	300	45	16
Zn_2SnO_4 cube	420	50	30	14
Zn_2SnO_4/C	563	60	40	14
Zn_2SnO_4/PPY	478.4	60	50	19
Zn_2SnO_4/graphene	326	50	40	24
Zn_2SnO_4/ZIF	349.2	500	20	25
Zn_2SnO_4/PANI	491.0	600	50	26
Our work(	577.4	100	50	
Mn_3O_4/Zn_2SnO_4	529.9	500	50	
composites)	441.5	1000	50	

The as-obtained 1D branched composites exhibit dramatically enhanced performance, including cycling stability, discharge–charge capacity and rate capability (see Table 1) when compared with most of Zn_2SnO_4-based anodes reported in the literature. The obvious improvement of the electrochemical performances might be attributed to the following four reasons: (i) its unique 1D structure facilitates the electrons transport during the processes of charging and discharging; (ii) the synergetic effects between Mn_3O_4 nanorods and Zn_2SnO_4 nanoneedles; (iii) the Zn_2SnO_4 nanoneedles are strongly anchored on the Mn_3O_4 nanorods to form an unique branched structure with good stability and integrity; (iv) the large degree of porosity of the composites enhances the electrolyte and Mn_3O_4/Zn_2SnO_4 electrode contact area and the open space between neighboring Zn_2SnO_4 nanoneedles ,which allows for easy diffusion of the electrolyte.[17]

Conclusions

In summary, novel 1D branched Mn_3O_4/Zn_2SnO_4 hierarchical composite of high yield has been prepared via a facile one-step hydrothermal route. It is evidenced that their formation is driven by the lattice match growth between cubic Mn_3O_4 and Zn_2SnO_4. The as-obtained product delivered a high first discharge capacity of 1370.9 mAh g^{-1}, and maintains a specific capacity of 577.4 mAh g^{-1} at a current density of 100 mA g^{-1} after 50 cycles. Their high initial capacity, excellent cycle stability and rate capability (even at a high current density of 1 A g^{-1}), are superior to other previously reported Zn_2SnO_4 materials. The excellent performance of these 1D branched composites can be mainly attributed to the hierarchical structures built by branches and tiny pores, and synergistic effect of different components. The method described here will open up a new pathway for the general synthesis variety of 1D hierarchical complex composites including Mn_3O_4 nanorod /$ZnFe_2O_4$ nanosheet (Fig. S5, S6) and $Mn_2O_3/CoFe_2O_4$ hierarchical composites (Fig. S7, S8) for diverse applications as high performance and high promising materials in energy, catalysis and environmental science and technology.

Supporting Information

Supporting Information is available online or from the author.

Acknowledgement

This research is financial support by and the 973 Project of China (No. 2011CB935901) and National Nature Science Fund of China and Academy of Sciences large apparatus United Fund (No.11179043).

Notes and references

Key Laboratory of Colloid & Interface Chemistry (Shandong University), Ministry of Education and School of Chemistry and Chemical Engineering, Shandong University, Jinan 250100, China
Fax: (+) 86-53188366280；Tel: (+) 86-53188364543；E-mail: xulq@sdu.edu.cn

1. M.V. Reddy, G.V. Subba Rao and B.V. R. Chowdari, *Chem. Rev.* , 2013,**113**, 5364-5457.
2. W. W. Zhou, C. W. Cheng, J. P. Liu, Y. Y. Tay, J. Jiang, X. T. Jia, J. X. Zhang, H. Gong, H. H. Hng, T. Yu and H. J. Fan, *Adv. Funct. Mater.*, 2011, **21**, 2439–2445.
3. J. Y. Liao, D. Higgins, G. Lui, V. Chabot, X. C. Xiao and Z. W. Chen, *Nano Lett.*, 2013, **13**, 5467−5473.
4. L. L. Xing, S. Yuan, B. He, Y. Y. Zhao, X. L. Wu and X. Y. Xue, *Chem. Asian J.*, 2013, **8**, 1530–1535.
5. H.H. Huang, J.W. Fang, Y. Xia, X.Y. Tao, Y. P. Gan, J. Du, W.J. Zhu and W.K. Zhang, *J. Mater. Chem. A.*, 2013, **1**, 2495-2500.
6. L. L. Li, S. J. Peng, Y. L. Cheah, J. Wang, P. F. Teh, Y. Ko, C. Wonga and M. Srinivasan, *Nanoscale*, 2013, **5**, 134-138.
7. S. M. Becker, M. Scheuermann, V. Sepelak, A. Eichhofer, D. Chen, R. Monig, A. S. Ulrich, H. Hahn and S. Indris, *Phys. Chem. Chem. Phys.*, 2011, **13**, 19624−19631.
8. X. H. Hou, Q. Cheng, Y. Bai and W. F. Zhang, *Solid State Ionics*, 2010, **181**, 631–634.
9. Y. Zhao, Y. Huang, Q. F. Wang, K. Wang, M. Zong, L. Wang, W. Zhang and X. Sun, *RSC Adv.*, 2013, **3**, 14480-14485.
10. K. Wang, Y. Huang, H. J. Huang, Y. Zhao, X. L. Qin, X. Sun, Y. L. Wang . *Ceramics International*, 2014, **40**, 8021-8025.
11. Y. W. Song, T. Y. Wen, L. L. Juan and L. J. Zhong, *Trans. Nonferrous Met. Soc. China*, 2012, **22**, 358-864.
12. X. X. Ji, X. T. Huang, Q. H. Zhao, A. H. Wang, X. Y. Liu, *Journal of Nanomaterials.*,2014,
13. Y. Zhao, Y. Huang, W. Zhang, Q. F. Wang, K. Wang, M. Zong, X. Sun, *RSC Advances,* 2013, **3**, 23489-23494.
14. K. Wang, Y. Huang, T. Z. Han, Y. Zhao, H. J. Huang and L. l. Xue, *Ceram. Int.*, 2014, **40**, 2359–2364.
15. L. H. Bao, J. F. Zang, X. D. Li, *Nano letters*, 2011, **11**,1215-1220.
16. X. Gu, L. Chen, Z. C. Ju, H. Y. Xu, J. Yang and Y. T. Qian, *Adv. Funct. Mater.*, 2013, **23**, 4049-4056.
17. C.Z. Yuan, H.B. Wu, Y. Xie and X.W. (David) Lou, *Angew. Chem. Int. Ed.*, 2013, **52**, 2-19.
18. Z. C. Bai, B. Sun, N, Fan, Z. C. Ju, M. H. Li, L. Q. Xu and Y. T. Qian, *Chem. Eur. J.*, 2012, **18**, 5319-5324.
19. B. J. Tan, K. J. Klabunde and P. M. A. Sherwood, *J. Am. Chem. Soc.*,1991, **113**, 855–861.
20. J. Goldberger, R. R. He, Y. F. Zhang, S. K. Lee, H. Q. Yan, H. J. Choi and P. d. Yang, *Nature*, 2003, **422,** 599-601.
21. C. Z. Yuan, H. B. Wu, Y. Xie and X. W. (David) Lou, *Angew, Chem. Int. Ed*, 2013, **52**, 2-19.
22. S. L, Li, A. H. Li, R. R. Zhang, Y. Y. He, Y. J. Zhai and L. Q. Xu, *Nano Research*, 2014, (DOI) 10.1007/s12274-014-0474-3.
23. Y. Ren, A. R. Armstrong, F. Jiao and P. G. Bruce, *J. Am. Chem. Soc.*, 2010, **132**, 996-101.
24. W. T. Song, J. Xie, S. Y. Liu, G. S. Cao, T. J. Zhu and X. B. Zhao, *J. Mater. Res.*, 2012, **27**, 3096-3102.
25. X. Z. Zheng, Y. F. Li, Y. X. Xu, Z. S. Hong and M. D. Wei, *CrystEngComm.*, 2012, **14**, 2112–2116.
26. Y. Zhao, Y. Huang，L. L. Xue, X. Sun, Q. F. Wang, W. Zhang, K. Wang and M. Zong, *Polym. Test.*, 2013, **32**, 1582–1587.